PNAS
www.pnas.org

Supplementary Information for

Flow-accelerated platelet biogenesis is due to an elasto-hydrodynamic instability

Christian Bächer, Markus Bender and Stephan Gekle

Christian Bächer.
E-mail: christian.baecher@uni-bayreuth.de

This PDF file includes:

Supplementary text
Figs. S1 to S21
Legends for Movies S1 to S5
SI References

Other supplementary materials for this manuscript include the following:

Movies S1 to S5

Supporting Information Text

S1. Methods - Details on the simulation method

A. Combined lattice-Boltzmann/immersed boundary method for active membranes. For the numerical investigation of blood platelet biogenesis we use a combined lattice-Boltzmann/immersed boundary method for active elastic membranes suspended in a 3D Newtonian fluid. We refer to our recent publication (3) for a detailed description of the algorithm. For extensive validation in case of active membranes as well as passive membrane we refer to ref. (3) and refs. (4, 5), respectively.

The dynamics of the suspending fluid is calculated on an Eulerian 3D grid by the mesoscopic lattice-Boltzmann method (6–8). Simulations are performed using the lattice-Boltzmann implementation in the software package ESPResSo (9–12) with the D3Q19 lattice-Boltzmann velocity set. A typical fluid mesh, as e.g. for the system shown in figure 3 a) of the main text, has dimensions of $720 \times 100 \times 40$. The time step is about 5×10^{-9} s and a typical total simulation time is 0.04 s. We assign to the suspending fluid a density of $1 \times 10^3\,\mathrm{kg/m^3}$ and a viscosity of 1.2×10^{-3} Pas, values resembling the properties of the *in vivo* environment of platelet formation, the blood plasma. Our LBM implementation furthermore allows for thermal fluctuations of the suspending fluid associated with a given temperature. In direction with no wall present, we use periodic boundary conditions. Walls are realized by the bounce back boundary condition. In the system shown in figure 3 a) we consider a channel with a height of 98 grid cells and apply a constant body force which corresponds to a pressure gradient driving Poiseuille flow. Velocities given in the text correspond to the maximum velocity of the corresponding flow profile. In figure 5 we apply a constant velocity to all fluid nodes surrounding the pillar, which leads to a homogeneous flow field. In figure S2 we apply a tangential velocity to the upper wall while the bottom remains steady. This leads to a pure linear shear flow.

The proplatelet membrane is discretized by nodes, which are separated by about one lattice-Boltzmann grid cell and connected to triangles. The resulting membrane mesh represents a Lagrangian grid immersed into the Eulerian fluid grid. Coupling of the membrane nodes to the fluid consists of the transmission of elastic membrane forces to the surrounding fluid nodes and advection of the membrane nodes with local fluid velocity (immersed boundary method (13–15)). In both cases an interpolation between membrane and fluid mesh is performed using an eight point stencil. A typical proplatelet membrane mesh consists of 22741 nodes and 45440 triangles and has a radius of approximately 6.25 LBM grid cells. If not stated explicitly the viscosity contrast of the fluid inside and outside the proplatelet is one. On its left hand side the proplatelet is fixed to a solid wall which mimics the fixed megakaryocyte *in vivo* or in experiments as illustrated in figure 1 a) of the main text. Fixation is done by an overlap of the last ring of the mesh with the solid boundary. As a consequence no fluid can enter/leave the proplatelet shaft. The terminal ring of nodes thus does not experience fluid forces and remains fixed. For stability reasons, in the last ring of nodes the calculation of active forces as well as bending forces is omitted.

The proplatelet membrane is attributed with different elastic properties. Shear elasticity associated with the cytoskeletal network underlining the plasma membrane is considered using the Skalak model (16, 17). We use the shear elasticity typical for red blood cell membranes $\kappa_S = 5 \times 10^{-6}$ N/m with $C = 100$ (18). Bending elasticity is modeled using Helfrich law (18–20) with a bending elasticity of $\kappa_B = 2 \times 10^{-19}$ Nm and realized by the algorithm denoted B in ref. (19). Activity of motor proteins walking on the cytoskeletal filaments is incorporated by actomyosin contractility as detailed in ref. (3).

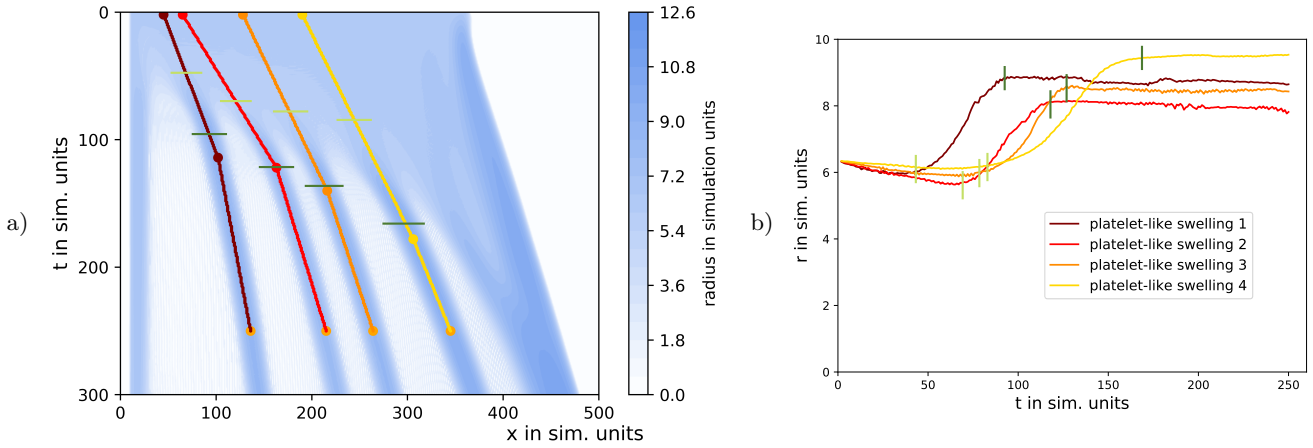

Fig. S1. Analysis of swelling formation. a) Kymograph showing the swelling formation along the shaft of a proplatelet. We track the position of the individual swellings indicated by the red to yellow lines in the kymograph. Out of the kymograph the local proplatelet radius over time is extracted leading to the profiles shown in figure b). Onset and duration of swelling formation are determined by the time step at which the deformation exceeds two percent of the initial radius (light green lines) and the time step at which the radius reaches a plateau (dark green lines).

B. Simulation analysis. *Kymograph* In order to visualize and analyze the temporal evolution of swelling formation we show kymographs of the proplatelet as e.g. in figure 2 d) or for an initial phase in figure S1 a). For the kymograph we analyze the local radius of the proplatelet depending on the position along the proplatelet axis. For this, we divide the nodes of the proplatelet mesh into bins along the proplatelet axis. In each bin, we first calculate the radial center-of-mass position and then determine the average radius over all nodes in the bin. With this we determine the radius depending on axial position for

each time step. For the kymograph we then plot the axial position on the abscissa and the time on the ordinate with time increasing downwards. Each point in the plot is colored according to the local radius at a given time.

Instability analysis In order to investigate the dynamics of swelling formation further we analyze the time course of swelling formation based on the kymograph. As shown in figure S1 a) each developing swelling manifests itself in a broad band with increased radius clearly separated from neighboring developing swellings. To analyze these dynamics we follow each developing swelling over time. We start from the initial configuration (dots at the top of figure S1 a)) and follow each maximum developing at the center of each swelling (red to yellow lines). As end point (dots at the bottom of figure S1 a)) we choose the time step when the local radius reaches a constant plateau. Taking the local radius from the kymograph for each point along the lines gives the time course of the local radius as shown in figure S1 b). Figure S1 b) clearly shows that swelling formation starts from a constant radius for all swellings and in the end terminates with a plateau.

From figure S1 b) we can furthermore calculate the onset time and the total duration of the instability. As onset we denote the time step at which the radius exceeds a deformation of two percent of the initial radius. Onsets for the different swellings are indicated by lines in light green in figure S1. As the end of the formation, we determine the time when the deformation reaches a plateau, as indicated by the dark green lines in figure S1. The time difference between these two stages gives the duration of the formation.

Platelet-sized swelling volume For each simulation we first determine the time of completed swelling development, as described above. At this time step, we calculate the volume of each swelling. This is done by considering just the swelling, where we have to close the membrane by triangles perpendicular to the proplatelet shaft. For the now closed platelet-like particle we can calculate the volume as described in reference (21). For each simulation we then filter for larger fragments, preplatelets, which form by swelling fusion. Eventually, we can calculate the average volume of all formed platelet-like particles.

S2. Varying flow geometries

A. Pure shear flow.

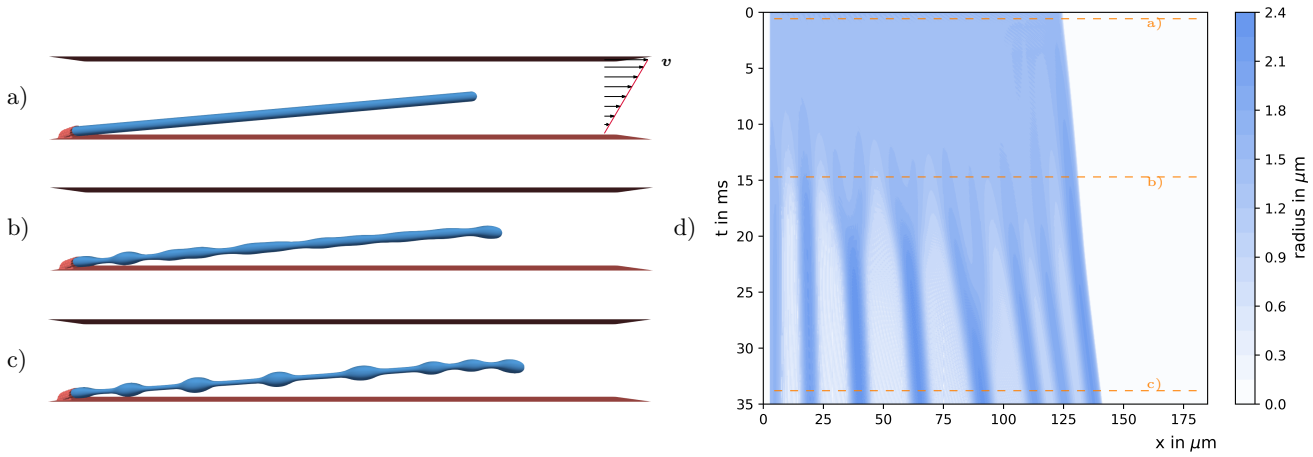

Fig. S2. Swelling fusion in shear flow. a) A proplatelet with the same properties as in the main text is immersed in a shear flow confined between two flat walls with velocity $v = 2$ mm/s. b), c) Simulation snapshots show the biological Rayleigh-Plateau instability and swelling fusion. The entire process is shown in Supplemental Video S3. d) Kymograph showing the dynamics of swelling formation and swelling movement along the shaft followed by several fusion events.

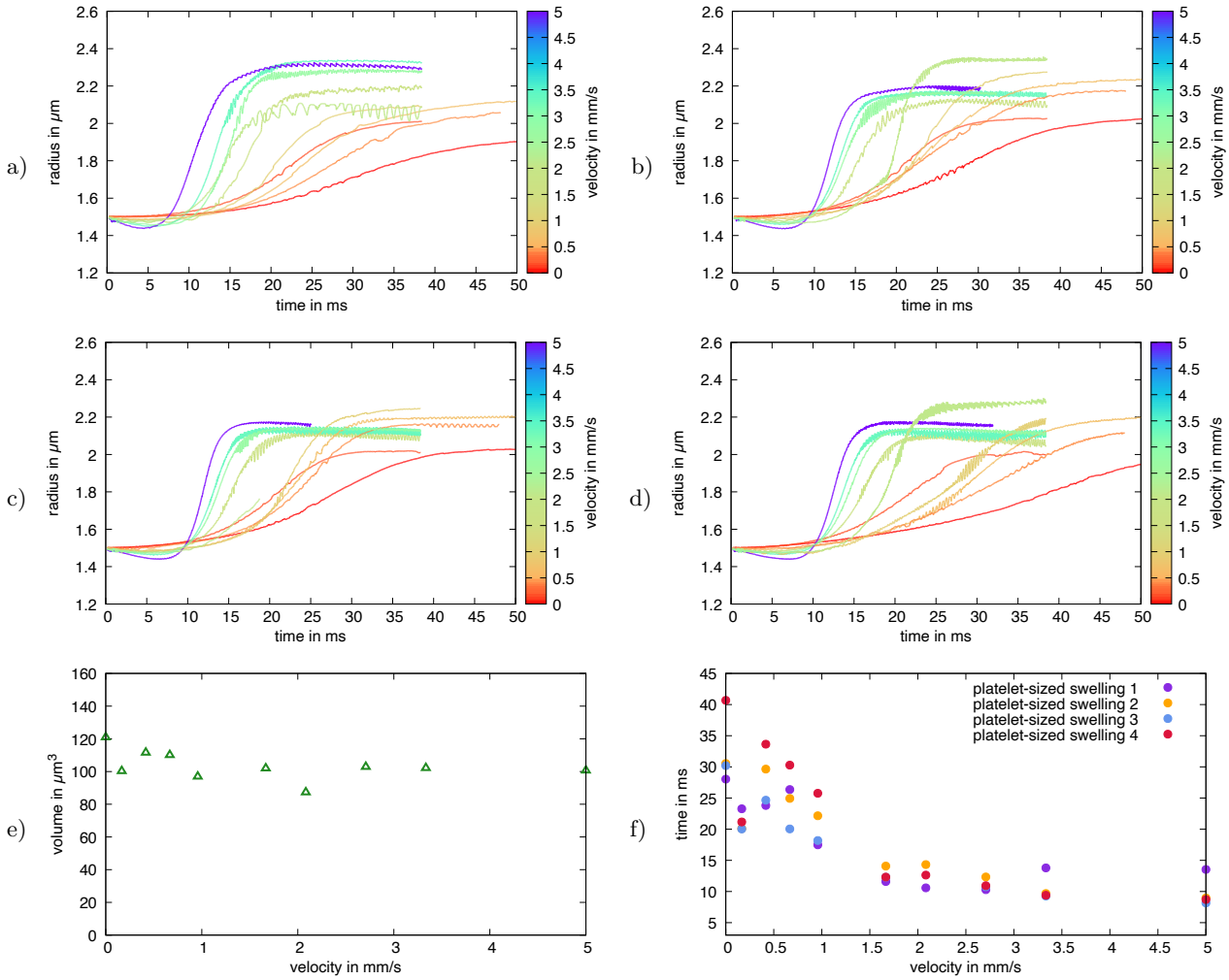

Fig. S3. Platelet biogenesis in shear flow. Time dependent formation process for a) first, b) second, c) third, and d) fourth swelling. The curves for different velocities are less broadly distributed, the formation process does not shift towards earlier times as strongly as it does in homogeneous flow. Systematic variation of the external flow velocity shows a nearly constant volume e) and a non-monotonous, less pronounced acceleration based on duration of swelling formation f).

B. Platelet biogenesis in a narrow blood vessel.

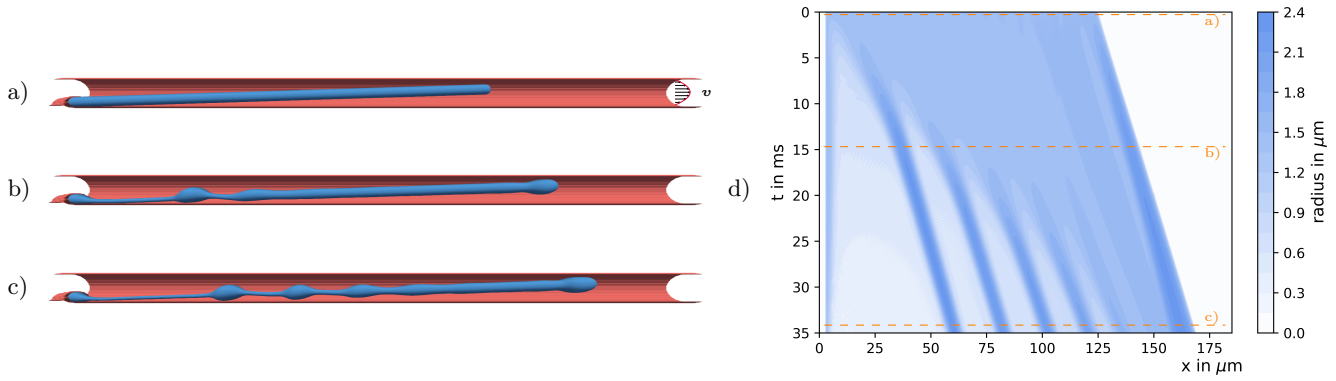

Fig. S4. Platelet biogenesis in a narrow blood vessel. a) A proplatelet with the same properties as in the main text is confined within a cylindrical channel with a diameter of 9 μm which corresponds to three times the proplatelet diameter. b) Under the action of the flow the proplatelet is extended and c) forms swellings via a biological Rayleigh-Plateau instability. The entire process is shown in Supplemental Video S5. d) Kymograph showing the dynamics of swelling formation.

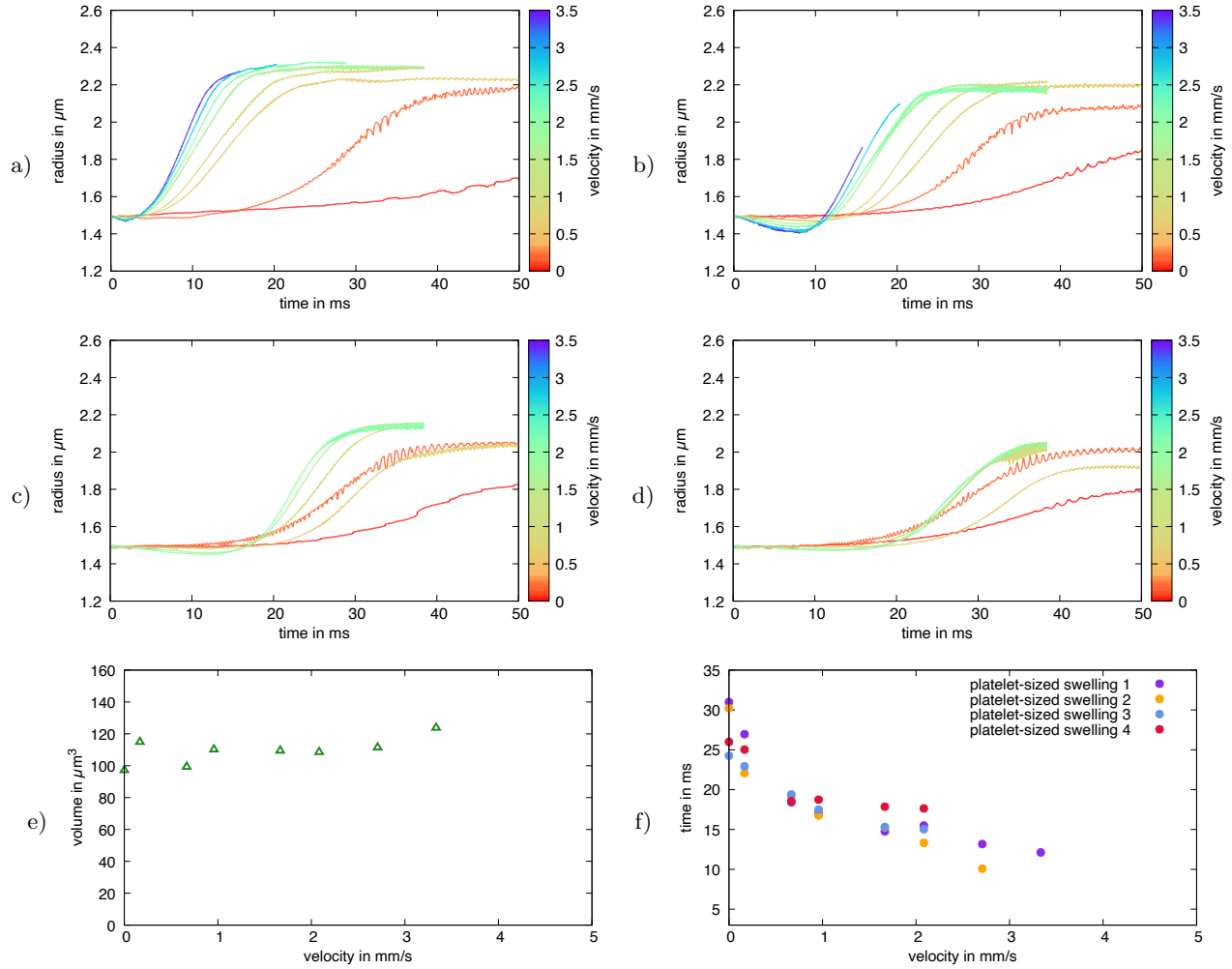

Fig. S5. Acceleration of platelet biogenesis in a narrow blood vessel. Time dependent formation process for a) first, b) second, c) third, and d) fourth swelling. The formation process shifts towards earlier times and time courses become steeper with increasing velocity. Systematic variation of the external flow velocity shows a nearly constant volume e) and systematic acceleration based on the duration of swelling formation f).

C. Additional data for homogeneous flow.

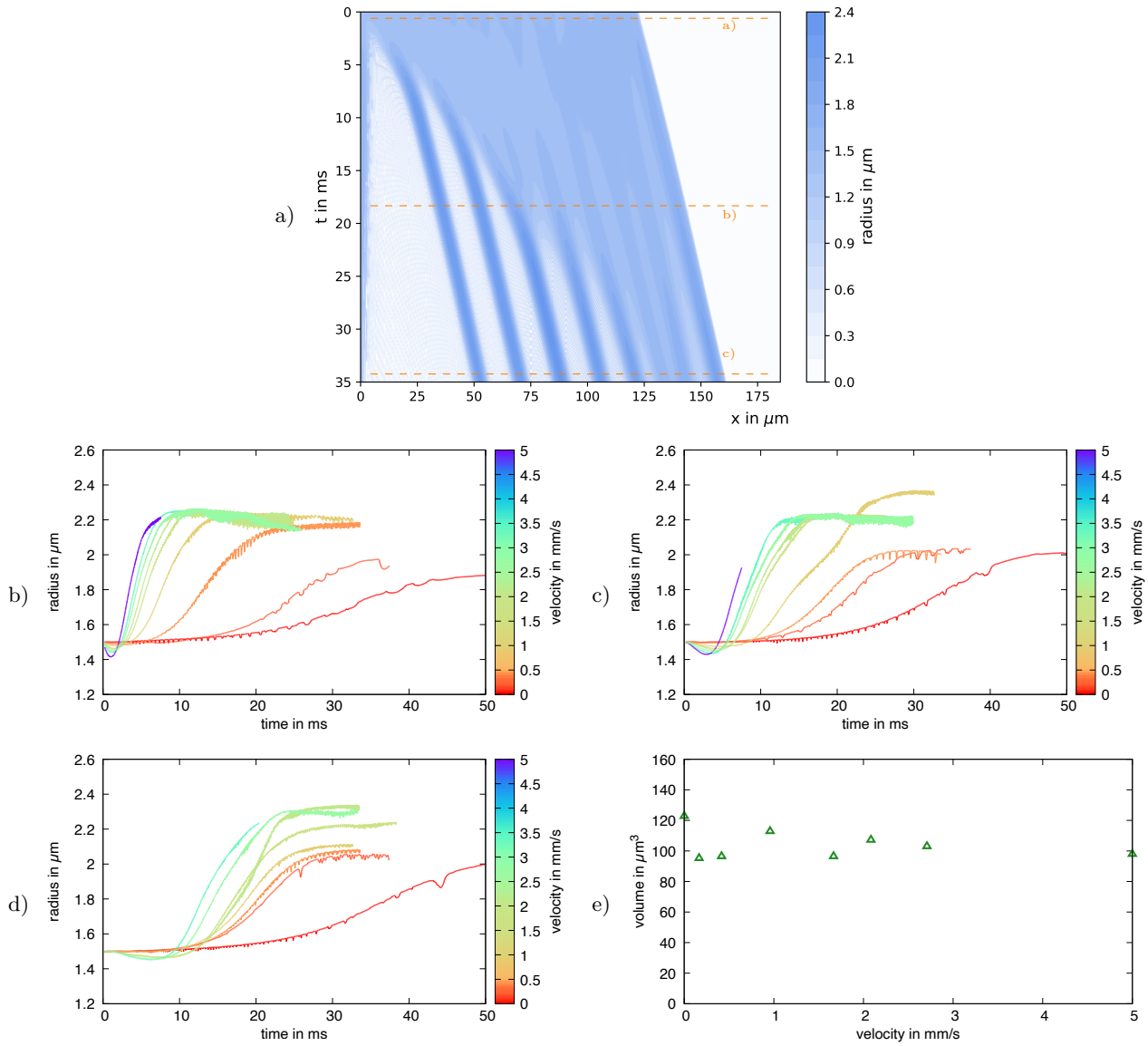

Fig. S6. Swelling formation in homogeneous flow. a) Kymograph corresponding to figure 5 of the manuscript shows the dynamics of swelling formation and swelling movement along the proplatelet shaft at uniform distances. b) - d) Time dependent formation process of the swellings. With increasing velocity the formation shifts towards shorter times and the slope of the curves becomes steeper. e) The volume stays constant over the whole range of velocities.

S3. Results for isotropic contractility

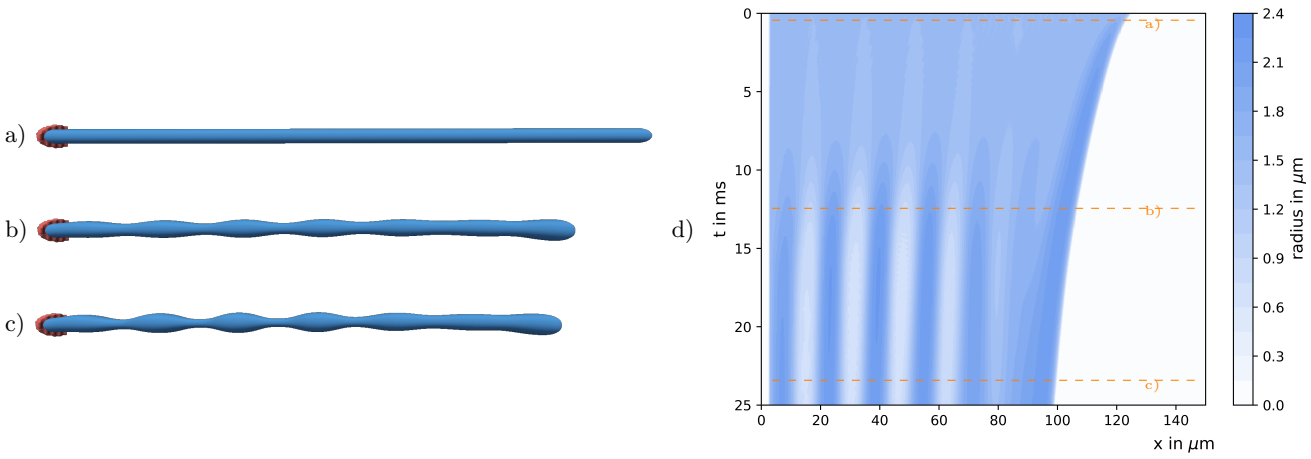

Fig. S7. Proplatelet fragmentation by a biological Rayleigh-Plateau instability for isotropic contractility without flow. a), b), c) the proplatelet undergoes a biological Rayleigh-Plateau instability and develops periodic swellings with a wavelength λ approximately satisfying the classical Rayleigh-Plateau criterion $2\pi R_0/\lambda \approx 0.69$. d) A kymograph illustrates the dynamics of swelling formation with the color coding for the local proplatelet radius. Time steps for the corresponding proplatelet shapes in figures a) - c) are indicated by the orange lines. Corresponding results for anisotropic contractility are shown in figure 2 of the manuscript.

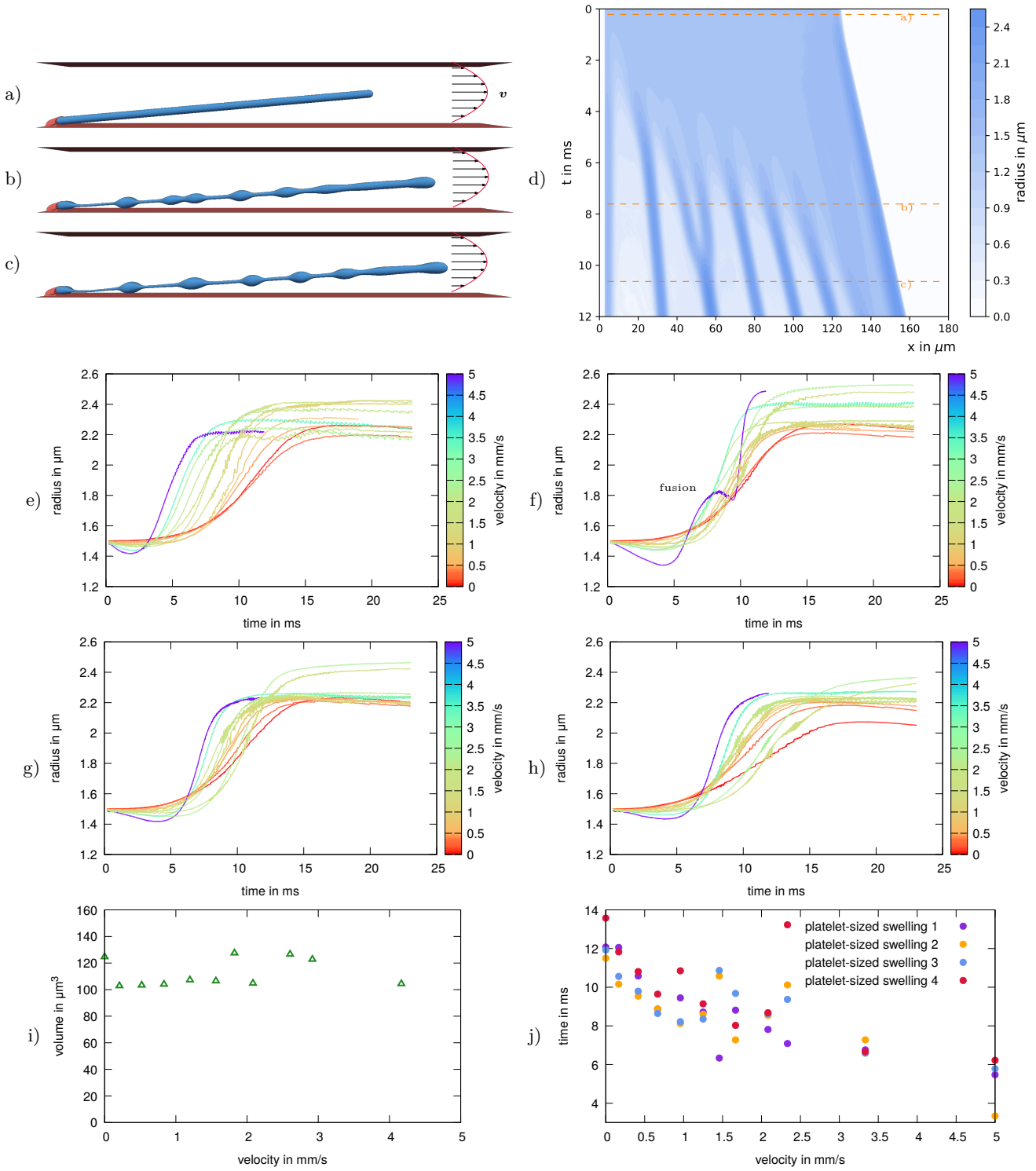

Fig. S8. Blood platelet biogenesis for isotropic contractility in Poiseuille flow. Blood platelet biogenesis in a channel with a parabolic Poiseuille flow with maximum velocity of $v = 5$ mm/s. a) A proplatelet is subject to an external Poiseuille flow confined between two walls. Due to the action of the flow the proplatelet extends b), swellings form, and the final platelet-sized swellings move at non-uniform distance along the proplatelet shaft c). d) The corresponding kymograph shows the dynamics of swelling formation and the motion of the final swellings. Two initially separated platelet-sized swellings fuse at around 10 ms. e), f), g), h) Time course of platelet-sized swelling formation in Poiseuille flow for e) first, f) second, g) third, and h) fourth swelling at varying external flow velocity. i) Swelling volume stays nearly constant over the whole range of velocities. j) With increasing flow velocity the duration time of the biological Rayleigh-Plateau instability / of swelling formation strongly accelerates. Corresponding results for anisotropic contractility are shown in figure 3 and 4 of the manuscript.

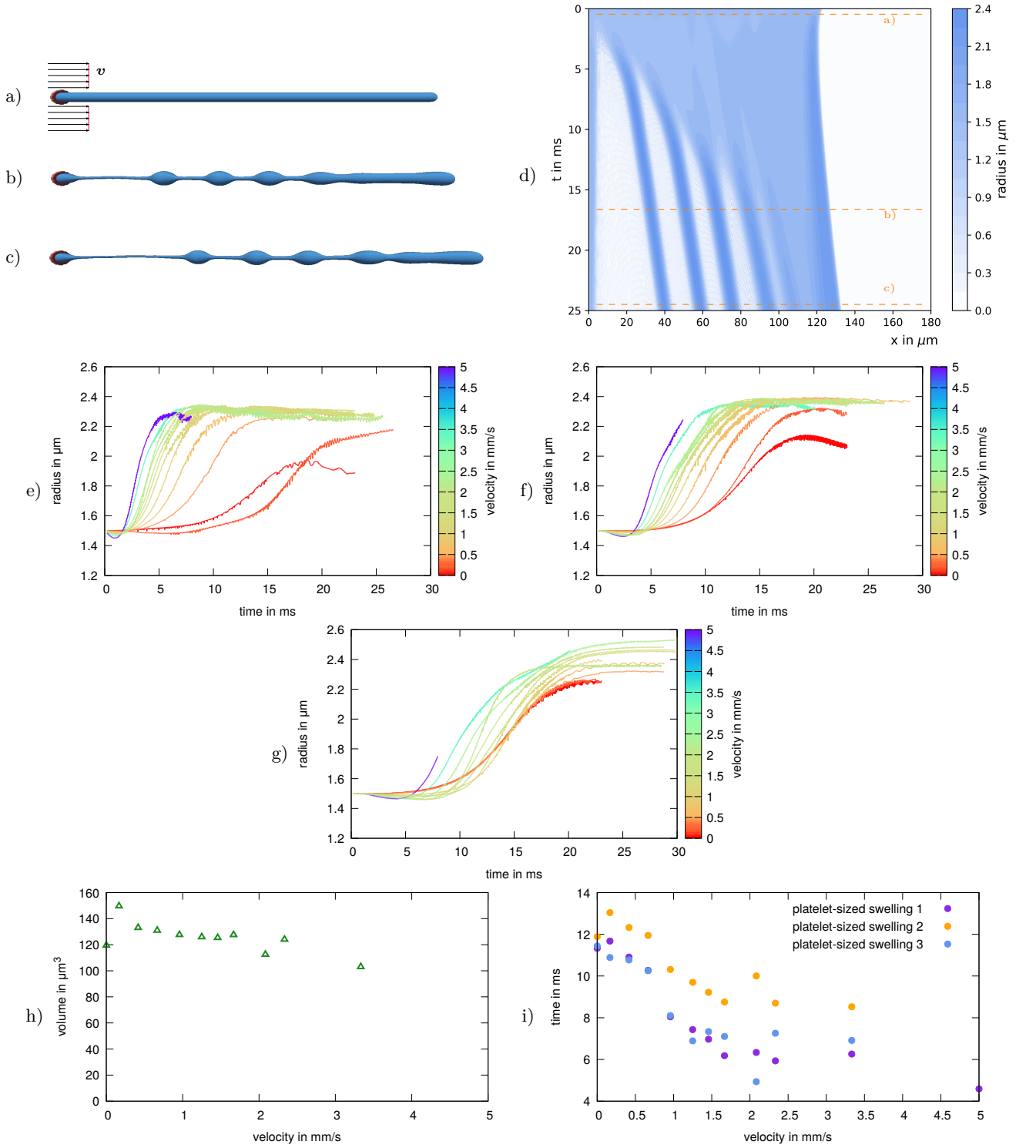

Fig. S9. Blood platelet biogenesis for isotropic contractility in homogeneous flow. Swelling formation in homogeneous flow with $v = 2.0$ mm/s. a) A proplatelet is immersed in a homogeneous flow and attached to a wall on the left hand side. b), c) The proplatelet undergoes a biological Rayleigh-Plateau instability while being extended by the homogeneous flow. d) Kymograph showing the dynamics of swelling formation and swelling movement along the proplatelet shaft at uniform distances. e), f), g) Time dependent formation process for e) first, f) second, and g) third swelling. With increasing velocity the formation shifts towards shorter times and the slope of the curves becomes steeper. No fusion events are visible. Systematic variation of the external flow velocity hardly affects the swelling volume h), but shows a strong acceleration of the duration of swelling formation i). Corresponding results for anisotropic contractility are shown in figure 5 of the manuscript and figure S6.

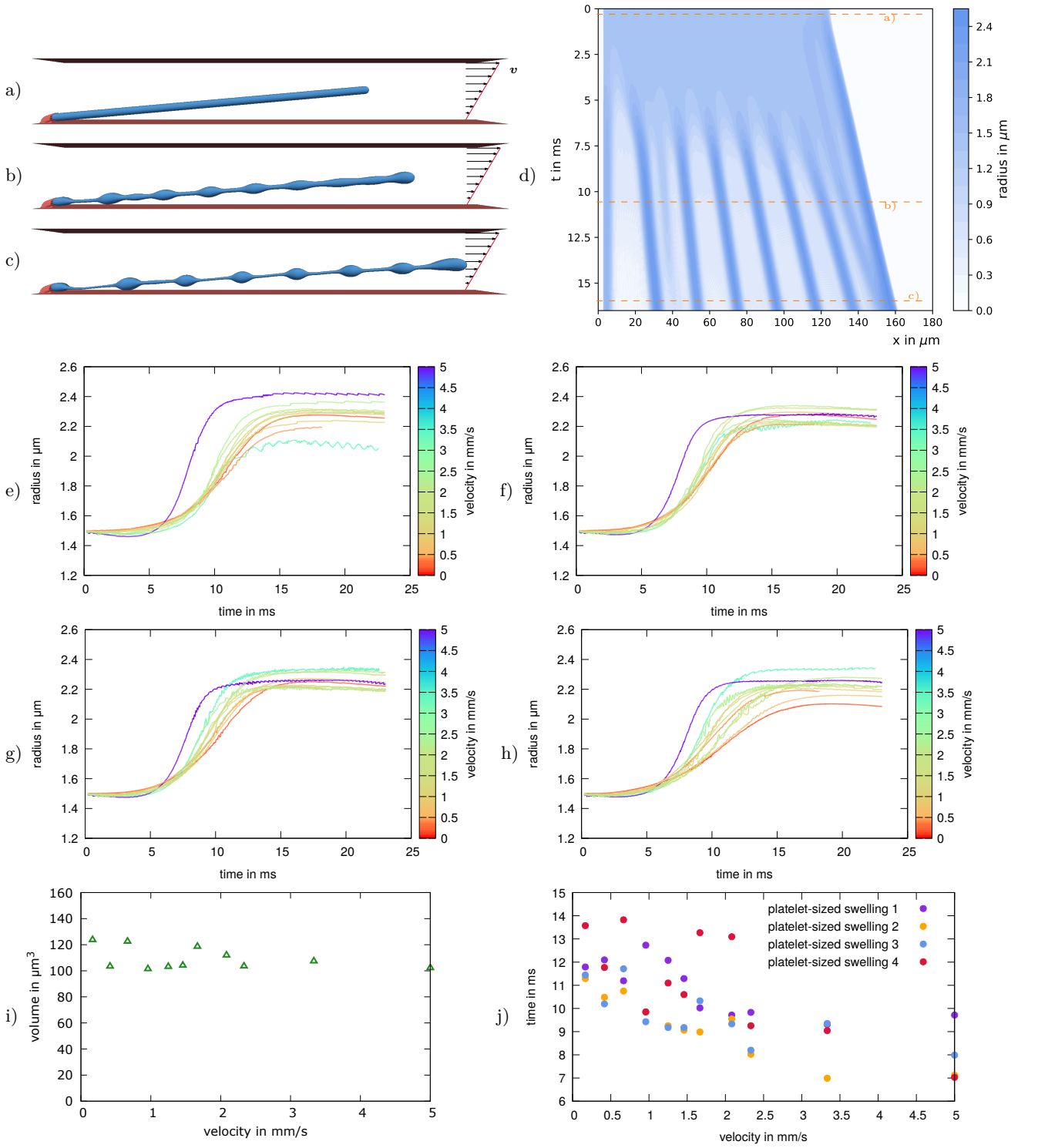

Fig. S10. Platelet biogenesis for isotropic contractility in shear flow. a) A proplatelet is immersed in a shear flow confined between two flat walls with velocity $v = 9$ mm/s. b), c) Simulation snapshots show the biological Rayleigh-Plateau instability and swelling fusion. d) Kymograph showing the dynamics of swelling formation and swelling movement along the shaft followed by fusion events at the first swelling and at the tip. e), f), g) h), Time dependent formation process for e) first, f) second, g) third, and h) fourth swelling. The curves for different velocities are less broadly distributed, the formation process does not shift towards earlier times as strongly as it does in homogeneous flow. Systematic variation of the external flow velocity shows a nearly constant volume e) and a non-monotonous, less pronounced acceleration based on duration of swelling formation f). Corresponding results for anisotropic contractility are shown in figure S2 and S3.

S4. Robustness against parameter variations

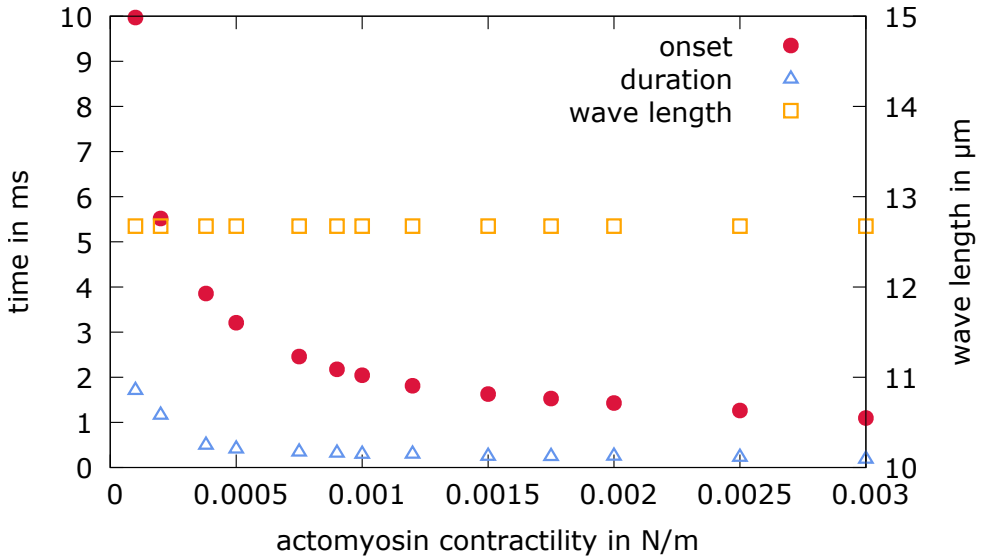

Fig. S11. Magnitude of actomyosin contractility. Towards smaller contractility an exponential increase in onset and duration is observed for a periodic cylindrical membrane. The instability wavelength however does not change with varying contractility.

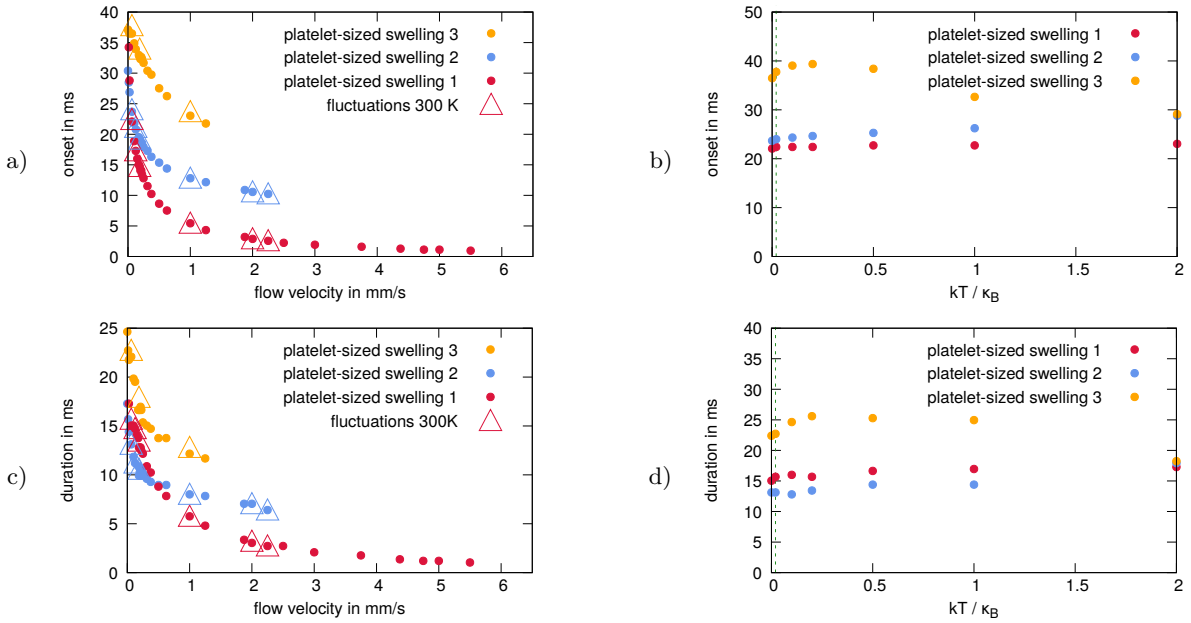

Fig. S12. Fluctuations do not influence instability dynamics. a) Onset time depending on the flow velocity of a homogeneous flow without (dots) and with (triangles) thermal fluctuations. b) For given velocity the temperature is systematically varied. c) Duration time depending on the flow velocity of a homogeneous flow without (dots) and with (triangles) thermal fluctuations. d) For given velocity the temperature is systematically varied. In total, the instability dynamics is not influenced in presence of thermal fluctuations. This can be explained by the initial proplatelet shape not being an unstable fix point, but proplatelet dynamics directly sets in.

a) $\eta_{\text{in}}/\eta_{\text{out}} = 1, v \approx 0.13$ mm/s

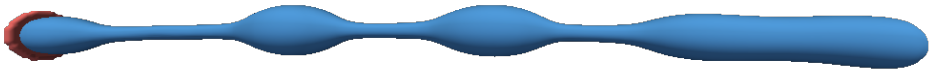

b) $\eta_{\text{in}}/\eta_{\text{out}} = 5, v \approx 0.13$ mm/s

c) $\eta_{\text{in}}/\eta_{\text{out}} = 1, v \approx 0.5$ mm/s

d) $\eta_{\text{in}}/\eta_{\text{out}} = 5, v \approx 0.5$ mm/s

e)

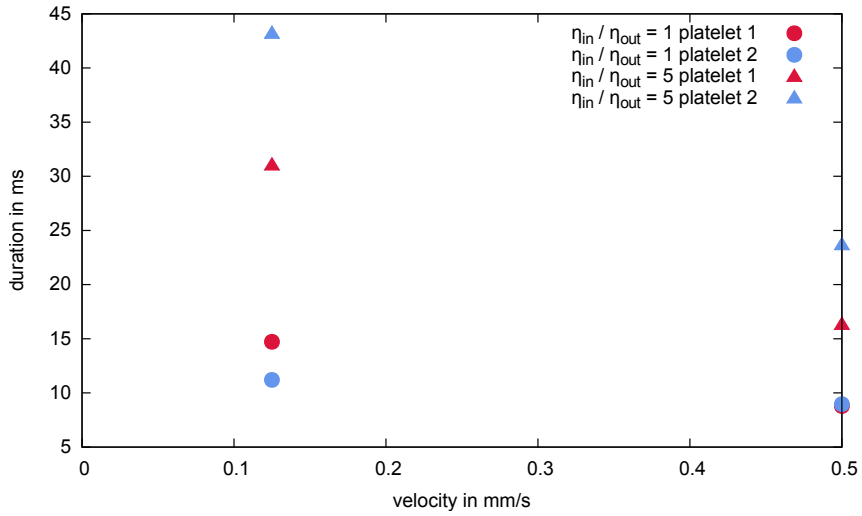

Fig. S13. Viscosity contrast increases instability duration. We compare swelling formation for isotropic actomyosin contractility in homogeneous flow at viscosity contrast of one at intermediate (a) and high (c) velocity to swelling formation at viscosity contrast of five in b) and d) for the same two velocities. Snapshots are shown at same time steps and thus comparison shows that swelling formation is slower for increased viscosity contrast. e) Quantitative comparison confirms that duration increases for higher viscosity contrast.

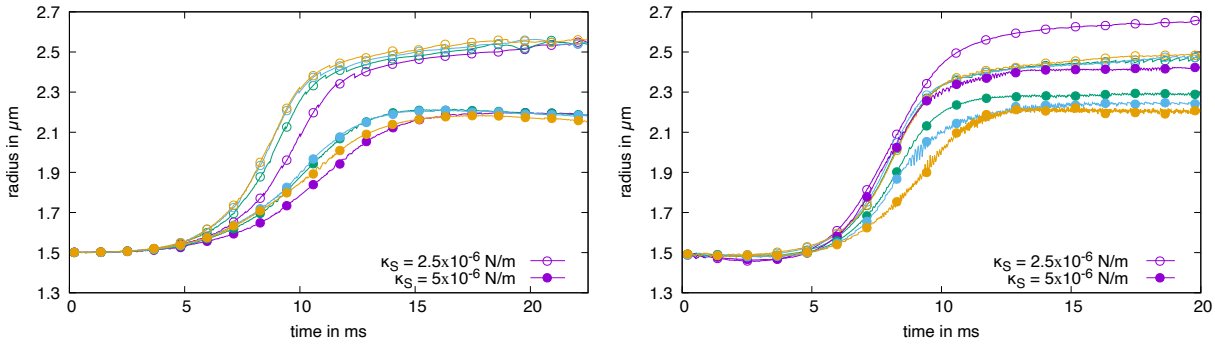

Fig. S14. Influence of shear elasticity. Comparison of simulations with two values of the shear elasticity: $k_{\mathrm{S}} = 5 \cdot 10^{-6}$N/m (as in the main text) and $k_{\mathrm{S}} = 2.5 \cdot 10^{-6}$N/m. Curves show the dynamic formation over time of platelet-sized swelling one (violet), two (green), three (blue), four (orange). Simulations are carried out for a) a small velocity $v = 0.167$ mm/s and b) a larger velocity $v = 1.67$ mm/s. Except for a slight difference in the proplatelet height, which is due to stronger relative contraction driven by actomyosin contractility, the formation process is not influenced.

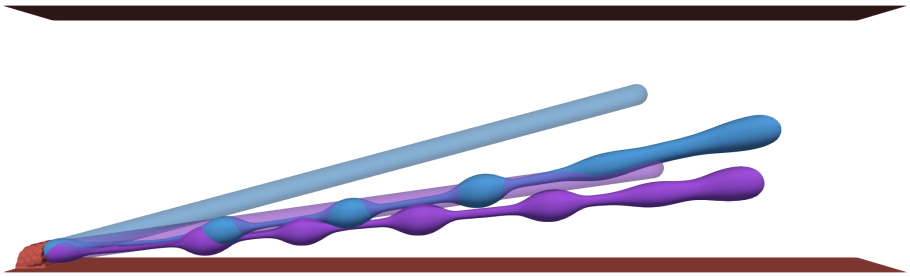

Fig. S15. Influence of the initial proplatelet angle in Poiseuille flow. Corresponding shapes for two different initial angles (different colors) are shown at the beginning and at one fixed time point in transparent and solid color, respectively. The less tilted proplatelet is stretched more strongly, but the overall behavior (number and size of swellings) remains the same.

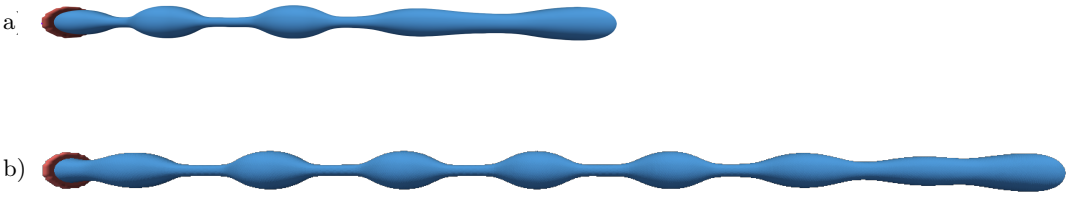

Fig. S16. Varying proplatelet length in simulation. a) A shorter and b) a longer proplatelet undergoing a biological Rayleigh-Plateau instability is simulated with a length 65 and 97 times the radius, respectively. The size of the swellings formed is the same in both simulations, we find a ratio $\frac{2\pi}{\lambda} R_0$ of 0.63 in a) and of 0.65 in b) together with a value of 0.66 for figure S7, which matches the result expected from the classical Rayleigh-Plateau theory 0.69 very well (22).

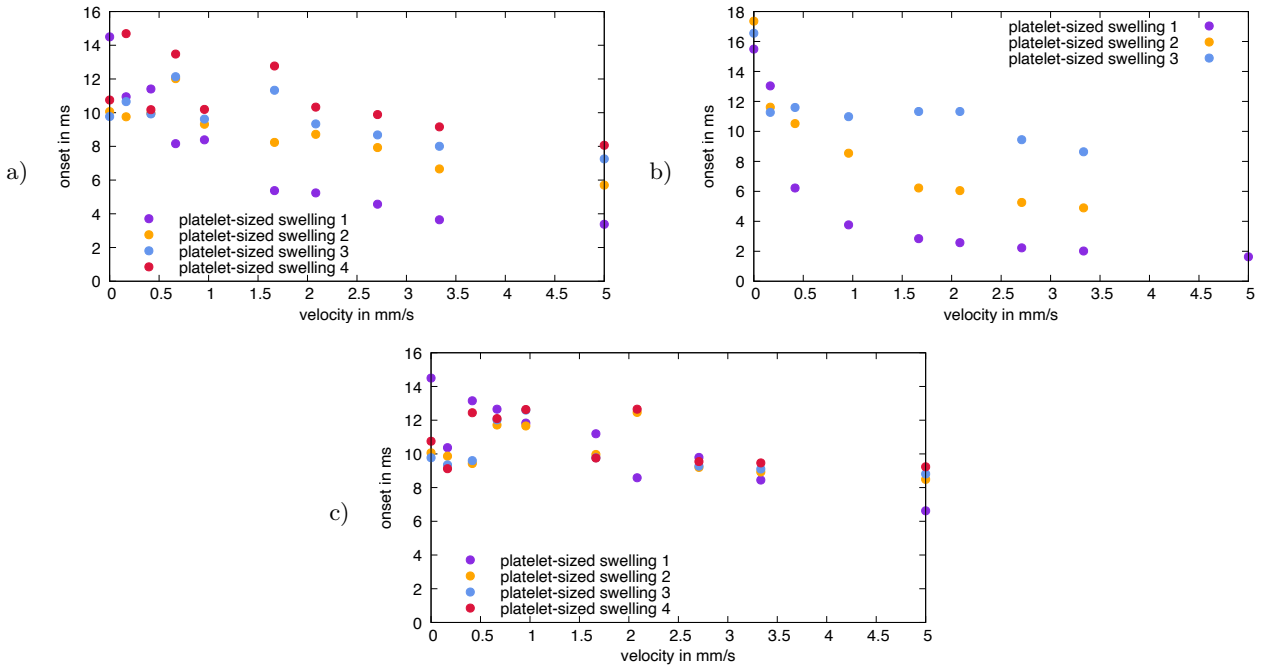

Fig. S17. Instability onset. Onset time of the instability depending on the flow velocity of a) Poiseuille flow, b) homogeneous flow, and c) shear flow. The instability onset can shift to earlier times, which is especially pronounced in the homogeneous flow in b).

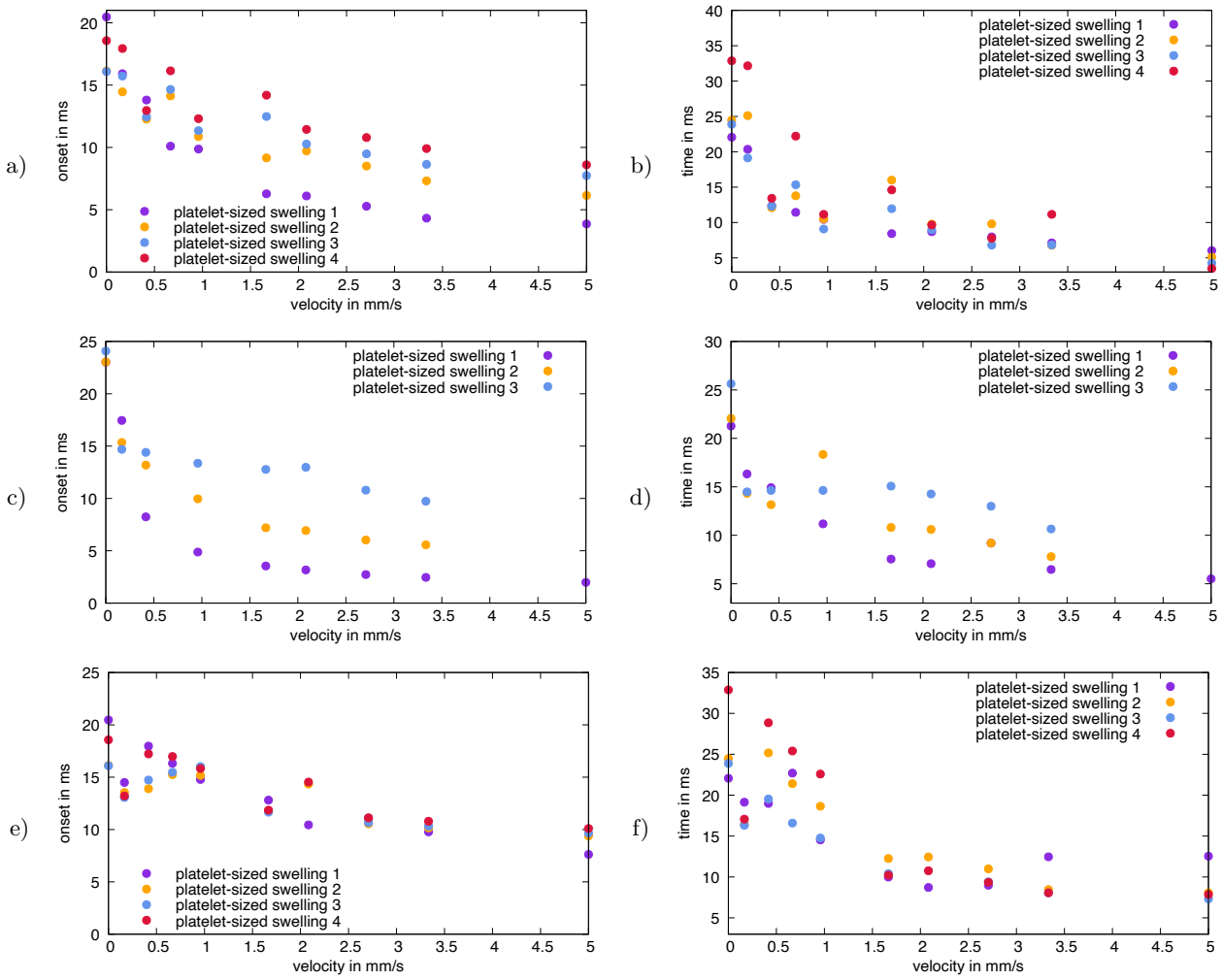

Fig. S18. Onset criterion of 5%. Considering a deformation of 5% of the initial proplatelet radius as criterion for instability onset does not affect the results in the manuscript for a criterion of 2%. In figure a) and b) we show the onset and duration for Poiseuille flow, as done in figure 4 of the manuscript. In figure c) and d) we show the onset and duration for homogeneous flow, as done in figure 5 of the manuscript. In figure e) and f) we show the onset and duration for shear flow, as done in figure S3. Onset shifts to longer times due to the larger deformation to be reached and duration reduces because of the reduced difference in time between onset and reaching a plateau. However, the dependency on flow velocity does not change.

S5. Fragmentation of released preplatelet

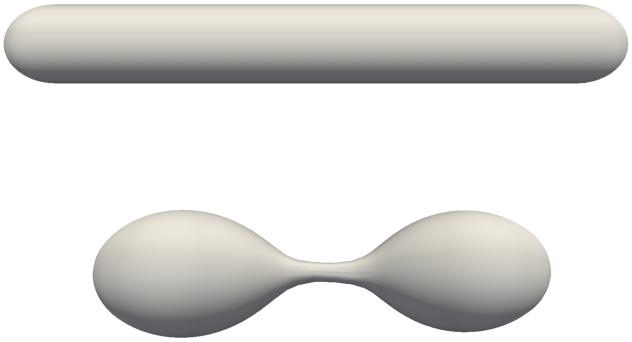

Fig. S19. Transition of a free, extended preplatelet. An already extended preplatelet undergoes a biological Rayleigh-Plateau instability and fragments into two separate platelets.

S6. Additional experimental data

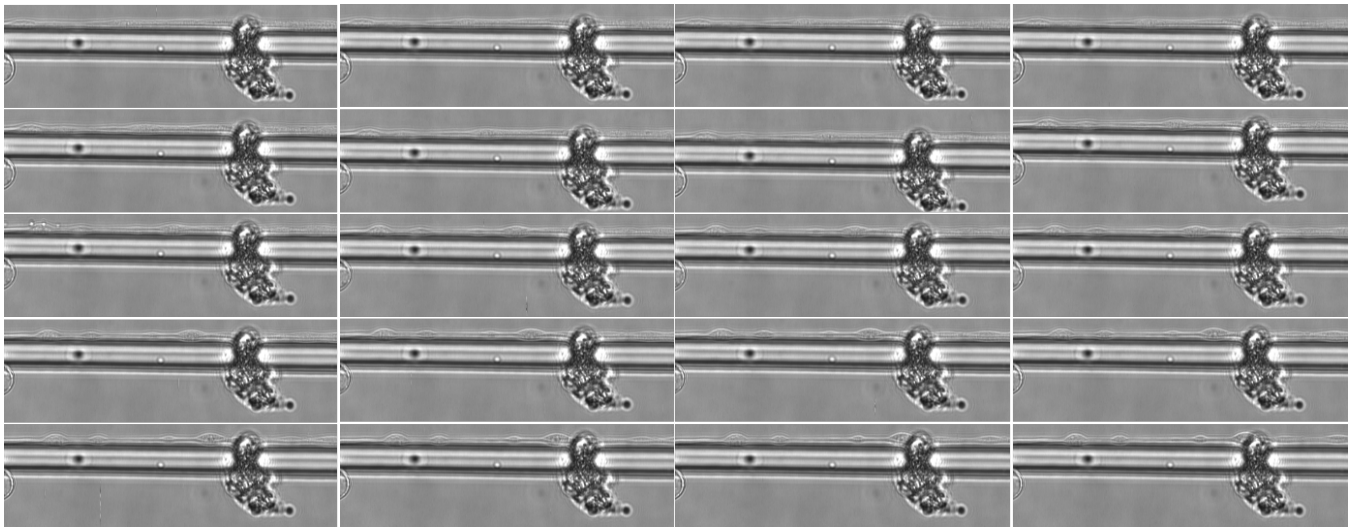

Fig. S20. Detailed time series of swelling formation observed in experiment. Images are taken every every five seconds, shown from left to right and from top to bottom, and image width corresponds to 137.5 μm. The initial extended proplatelet is shown in the top left corner and the eventual proplatelet with swellings formed in the bottom right corner.

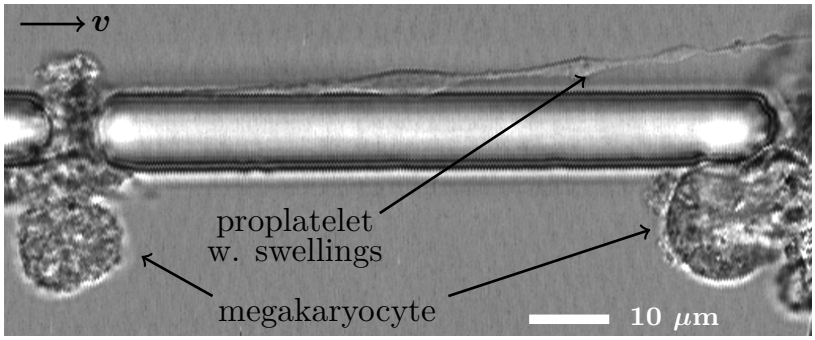

Fig. S21. Periodic arrangement of the Megakaryocytes. Megakaryocytes are trapped in the bottom part of a microfluidic bioreactor in periodically arranged gaps. The left megakaryocyte extends a proplatelet, which forms periodic swellings. Fluid flows with a maximum velocity of 2.2 mm/s and the complete width of the experimental image is 100.81 μm.

Movie S1. Proplatelet undergoing a biological Rayleigh-Plateau instability in a quiescent fluid. Movie corresponding to figure 2 of the manuscript.

Movie S2. Proplatelet undergoing a biological Rayleigh-Plateau instability in a parabolic Poiseuille flow with maximum velocity of $v = 3.33$ mm/s. Movie corresponding to figure 3 of the manuscript.

Movie S3. Proplatelet undergoing a biological Rayleigh-Plateau instability in a shear flow with velocity $v = 2.0$ mm/s. Movie corresponding to figure S2.

Movie S4. Proplatelet undergoing a biological Rayleigh-Plateau instability in a homogeneous flow with constant velocity $v = 2.0$ mm/s. Movie corresponding to figure 5 of the manuscript and figure S6.

Movie S5. Proplatelet undergoing a biological Rayleigh-Plateau instability in a narrow blood vessel with a maximum velocity of $v = 2.0$ mm/s. Movie corresponding to figure S4 and S5.

References

1. JL Villeval, et al., High Thrombopoietin Production by Hematopoietic Cells Induces a Fatal Myeloproliferative Syndrome in Mice. *Blood* **90**, 4369–4383 (1997).
2. JN Thon, et al., Platelet bioreactor-on-a-chip. *Blood* **124**, 1857–1867 (2014).
3. C Bächer, S Gekle, Computational modeling of active deformable membranes embedded in three-dimensional flows. *Phys. Rev. E* **99**, 062418 (2019).
4. C Bächer, L Schrack, S Gekle, Clustering of microscopic particles in constricted blood flow. *Phys. Rev. Fluids* **2**, 013102 (2017).
5. C Bächer, et al., Antimargination of Microparticles and Platelets in the Vicinity of Branching Vessels. *Biophys. J.* **115**, 411–425 (2018).
6. B Dünweg, AJ Ladd, Lattice Boltzmann simulations of soft matter systems in *Advanced Computer Simulation Approaches for Soft Matter Sciences III.* (Springer), pp. 89–166 (2009).
7. CK Aidun, JR Clausen, Lattice-Boltzmann Method for Complex Flows. *Annu. Rev. Fluid Mech.* **42**, 439–472 (2010).
8. T Krüger, et al., *The Lattice Boltzmann Method: Principles and Practice.* (Springer), (2016).
9. H Limbach, A Arnold, B Mann, C Holm, ESPResSo—an extensible simulation package for research on soft matter systems. *Comput. Phys. Commun.* **174**, 704–727 (2006).
10. D Roehm, A Arnold, Lattice Boltzmann simulations on GPUs with ESPResSo. *The Eur. Phys. J. Special Top.* **210**, 89–100 (2012).
11. A Arnold, et al., ESPResSo 3.1: Molecular Dynamics Software for Coarse-Grained Models in *Meshfree Methods for Partial Differential Equations VI.* (Springer, Berlin, Heidelberg), pp. 1–23 (2013).
12. F Weik, et al., ESPResSo 4.0 – an extensible software package for simulating soft matter systems. *The Eur. Phys. J. Special Top.* **227**, 1789–1816 (2019).
13. CS Peskin, The immersed boundary method. *Acta Numer.* **11**, 479–517 (2002).
14. R Mittal, G Iaccarino, Immersed Boundary Methods. *Annu. Rev. Fluid Mech.* **37**, 239–261 (2005).
15. L Mountrakis, E Lorenz, AG Hoekstra, Revisiting the use of the immersed-boundary lattice-Boltzmann method for simulations of suspended particles. *Phys. Rev. E* **96**, 013302 (2017).
16. R Skalak, A Tozeren, RP Zarda, S Chien, Strain energy function of red blood cell membranes. *Biophys. J.* **13**, 245 (1973).
17. D Barthès-Biesel, Motion and Deformation of Elastic Capsules and Vesicles in Flow. *Annu. Rev. Fluid Mech.* **48**, 25–52 (2016).
18. JB Freund, Numerical Simulation of Flowing Blood Cells. *Annu. Rev. Fluid Mech.* **46**, 67–95 (2014).
19. A Guckenberger, MP Schraml, PG Chen, M Leonetti, S Gekle, On the bending algorithms for soft objects in flows. *Comput. Phys. Commun.* **207**, 1–23 (2016).
20. A Guckenberger, S Gekle, Theory and algorithms to compute Helfrich bending forces: A review. *J. Physics: Condens. Matter* **29**, 203001 (2017).
21. Cha Zhang, Tsuhan Chen, Efficient feature extraction for 2D/3D objects in mesh representation in *Proceedings 2001 International Conference on Image Processing (Cat. No.01CH37205).* (IEEE, Thessaloniki, Greece), Vol. 2, pp. 935–938 (2001).
22. J Eggers, E Villermaux, Physics of liquid jets. *Reports on Prog. Phys.* **71**, 036601 (2008).